OPTICA

Spatiotemporal plasma hologram

Zhaohui Wu,[1] Xiaoming Zeng,[1] Zhaoli Li,[1] Xiaodong Wang,[1] Jie Mu,[1] Hao Peng,[2,6] Kainan Zhou,[1] Dongxia Hu,[1,7] Yanlei Zuo,[1,8] Nathaniel J. Fisch,[3] Caterina Riconda,[4] and Stefan Weber[5,9]

[1]National Key Laboratory of Plasma Physics, Research Center of Laser Fusion, China Academy of Engineering Physics, Mianyang, Sichuan 621900, China
[2]Shenzhen Key Laboratory of Ultraintense Laser and Advanced Material Technology, Center for Advanced Material Diagnostic Technology, and College of Engineering Physics, Shenzhen Technology University, Shenzhen 518118, China
[3]Department of Astrophysical Sciences, Princeton University, Princeton, New Jersey 08543, USA
[4]LULI, Sorbonne Université, CNRS, École Polytechnique, CEA, F-75005 Paris, France
[5]ELI Beamlines Facility, Extreme Light Infrastructure ERIC, 25241 Dolni Brezany, Czech Republic
[6]penghao@sztu.edu.cn
[7]dongxia.hu@163.com
[8]zuoyanlei@tsinghua.org.cn
[9]Stefan.Weber@eli-beams.eu

Received 31 October 2025; revised 8 May 2026; accepted 11 May 2026; published 22 May 2026

Holography enables simultaneous recording, storage, and processing of both amplitude and phase information in optical fields, making it a versatile technique with broad applications across multiple disciplines. However, current holographic techniques still lack the ability to capture temporal information. Here, based on plasma grating generated by spatially varying ionization, we experimentally realize a spatiotemporal volume hologram, enabling femtosecond-resolved recording, storage, and retrieval of both spatial and temporal information from an object pulse. Using two complementary probing schemes—multi-shot scanning with a focused probe and single-shot imaging with an expanded probe—we reliably reconstruct complex spatiotemporal structures, including Gaussian and Laguerre–Gaussian beams. The scheme's robustness has been thoroughly characterized by investigating the operational intensity range of the object pulse and hologram lifetime. These results create possibilities for ultrafast optical memory devices and real-time signal processors, potentially enabling applications in high-speed optical communications and analog computing.

https://doi.org/10.1364/OPTICA.583469

1. INTRODUCTION

Holography encodes both phase and amplitude information of an object pulse through refractive index modulations created by interference with a reference pulse in a photosensitive medium. Three-dimensional reconstruction is achieved using a delayed reference beam, enabling applications in optical metrology [1], 3D displays [2], sensing [3], and pump-probe microscopy [4]. In recent years, plasma hologram was proposed due to its fast response speed and high damage threshold. In plasma optics [5,6], plasma holograms can be generated via ponderomotive forces or spatially varying ionization (SVI), either on solid plasma surfaces [7] or in underdense volume plasmas [8,9]. The ultrahigh damage threshold of plasma enables these holograms to function as robust optical elements—when illuminated by an intense probe pulse, they can generate relativistic-intensity replicas of weak object pulses. This unique capability allows plasma holograms to serve as efficient mode converters [7,8] or compact holographic lenses [9] for high-power laser applications.

However, the holograms mentioned above lack the capacity to record temporal information, as they are fundamentally limited to spatial encoding. As proposed by Dodin and Fisch [10,11], the temporal information together with the spatial information of the object pulse can be stored into a slow propagating plasma Langmuir wave by the Raman scattering with a short reference pulse in a plasma and further retrieved with a probe pulse. This time-resolved hologram may render the development of interesting ultrafast optical memory cells, optical signal processors, etc. [12–14]. However, this spatiotemporal Raman plasma hologram faces practical limitations. First, the encoding speed is constrained by the Langmuir wave growth rate ($\gamma_{\mathrm{growth}} \ll \omega_{\mathrm{pe}}$), typically requiring 100s of femtoseconds. Moreover, the information storage duration is limited by the Langmuir wave's short lifetime [15]. These fundamental constraints currently restrict the technique's applicability compared to conventional spatial holography.

In this work, for the first time, we propose and experimentally demonstrate a spatiotemporal plasma hologram based on spatially varying ionization plasma grating. The temporal resolution, determined by the ultrashort reference pulse duration during collision with the object pulse, reaches femtosecond scales. Due to the plasma grating's high damage threshold, this also represents the

first experimental realization of spatiotemporal holography in the high-intensity regime.

2. SCHEME AND THEORETICAL MODEL

The scheme is illustrated in Fig. 1(a). An object pulse with a predefined spatiotemporal structure (left) is injected into the gas medium, counter-propagating with a much shorter reference pulse (right). As the reference pulse scans across the object pulse, their interference in the interaction zone ionizes the gas, creating plasma gratings. These gratings encode the object pulse's spatiotemporal information, as both the ionization probability and resulting plasma density are proportional to the local interference field amplitude. This process effectively captures a spatiotemporal "snapshot" of the object pulse, stored as a hologram in the standing plasma grating. Following a controlled delay before plasma relaxation [Figs. 1(b) and 1(c)], a short probe pulse is incident on the hologram. The probe can be either tightly focused onto a specific grating location or expanded to cover the entire holographic structure. In both configurations, diffraction occurs with an efficiency proportional to the local grating density, enabling readout of either localized or complete spatiotemporal information from the original object pulse.

The scheme can be theoretically modeled as follows: the interference pattern intensity is given as $I(\mathbf{r}, t) = c\varepsilon_0|\mathbf{E}_{\text{obj}}(\mathbf{r}, t) + \mathbf{E}_{\text{ref}}(\mathbf{r}, t)|^2/2$, where c is the speed of light in vacuum, ε_0 is the vacuum permittivity, $\mathbf{E}_{\text{obj}}(\mathbf{r}, t) = \mathbf{E}_0 T(x - ct)S(y, z)e^{i\phi(y,z)}e^{i(\omega t - kx)}$ is the electric field of the object pulse carrying the temporal information in the envelope $T(x - ct)$, transverse amplitude $S(y, z)$, and phase information $\phi(y, z)$, $\mathbf{E}_{\text{ref}}(\mathbf{r}, t) = \mathbf{E}_1\delta(x + ct)e^{i(\omega t + kx)}$ is the short reference pulse [10], respectively. The resulting standing wave modulation

$$\Delta I(\mathbf{r}) \propto E_0 E_1 T(2x)S(y, z)\cos[2kx - \phi(y, z)] \qquad (1)$$

induces plasma density modulations via multiphoton/tunneling ionization. The MO-PPT model calculations [16–21] (see details in Section 5) demonstrate that for air constituents (nitrogen and oxygen) at intensities below the first-electron saturation threshold, the time-integrated ionization probability during the reference pulse duration has a positive correlation with the local laser intensity. Thus, by operating at optimized intensities just below saturation (Table 1), we achieve a density modulation as $\Delta n_p(\mathbf{r})$, which is positively correlated with $\Delta I(\mathbf{r})$. This correlation enables complete spatiotemporal encoding in a plasma volume hologram with femtosecond-scale formation time, which is the order of magnitude faster than Raman-based approaches. The temporal resolution of the hologram is fundamentally limited only by the ~ 30 fs reference pulse duration, which permits faithful storage of the object pulse's fine temporal features.

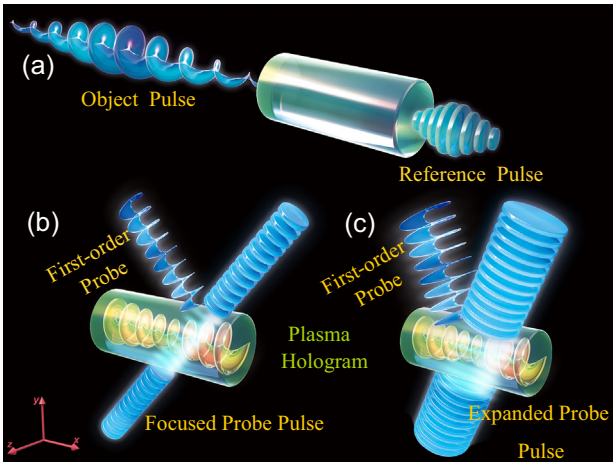

Fig. 1. Scheme of the spatiotemporal plasma hologram. (a) A long object pulse and a short counterpropagating reference pulse are focused into the ambient air and generate the plasma hologram by SVI. Retrieval of the spatiotemporal information of the object pulse with a focused probe (b) and an expanded probe (c).

After a picosecond-scale delay, a second-harmonic probe pulse—either focused or expanded—is injected at the Bragg angle $\theta_B = \sin^{-1}(\lambda_p/2\Lambda) \approx 30°$ with respect to the y axis in the xy plane, where $\Lambda = \lambda_0/2$ is the grating period, as shown in Figs. 1(b) and 1(c). The probe intensity was optimized to be sufficient for detection while remaining below the ionization threshold to avoid distorting the stored information. The probe diffracts into orders: the zero-order passes through unchanged(right), while the first-order(left) carries the reconstructed object-pulse information, which is then captured by a CCD camera. The diffracted intensity follows $I_{\text{diff}}(\mathbf{r}) = \eta(\mathbf{r})I_{\text{probe}}$, where the diffraction efficiency $\eta(\mathbf{r})$ depends on the plasma perturbation as $\eta(\mathbf{r}) = \sin^2[\Delta n(\mathbf{r})\pi L/\lambda_p \cos\theta_B]$ [22], where $\Delta n(\mathbf{r}) \approx \Delta n_p(\mathbf{r})/2n_c$ is the refractive index modulation related to the density modulation $\Delta n_p(\mathbf{r})$ and n_c is the critical density corresponding to the probe pulse. In our experimental configuration using a second-harmonic probe with oblique incidence, the short grating thickness L (approximately matching the object waist diameter) results in low diffraction efficiency. This allows us to employ the approximation:

$$\eta(\mathbf{r}) \approx \left[\Delta n(\mathbf{r})\pi L/\lambda_p \cos\theta_B\right]^2, \qquad (2)$$

yielding the relationship $I_{\text{diff}}(\mathbf{r}) \propto \Delta n_p^2(\mathbf{r})$, which enables direct mapping of the holographic information onto the probe's spatial intensity distribution. Numerical computations using the MO-PPT model and Eq. (2) reveal an approximately proportional relationship between the diffracted probe intensity and the object intensity [Fig. 4(e)]. This confirms that the probe pulse accurately reconstructs the object field's spatiotemporal distribution. Combined with the measured object energy, these results enable complete reconstruction of the object pulse's spatiotemporal intensity profile. Compared to Raman-based holograms, the SVI hologram exhibits substantially longer information storage, governed by plasma diffusion processes, which typically persist for 10s to 100s of picoseconds [23,24] (as discussed in detail later). Note that plasma volume gratings typically aim for manipulating ultra-intense laser with high diffraction efficiency [9,25–27], our work specifically focuses on information encoding and retrieval rather than high-efficiency diffraction of intense lasers.

3. EXPERIMENTAL RESULTS

With the experimental setup shown in Fig. 6 and primary parameters given in Table 1, we carried out the experiment for the spatiotemporal plasma hologram. We first demonstrate transverse spatial information retrieval by focusing the probe to the hologram at a fixed longitudinal position [Fig. 1(b)]. Two object pulses including a Gaussian pulse with flat phase and a Laguerre–Gaussian (LG) pulse (topological charge $m = 1$) with donut-shaped intensity and helical phase were used. The diffracted

Table 1. Key Experimental Parameters, Where E, λ, I, τ, and W Represent the Laser Energy, Central Wavelength, Peak Intensity, Full Width at Half-Maximum Duration and Waist Diameter, Respectively

Parameters	E (mJ)	λ (μm)	I (W/cm^2)	τ (fs)	W (μm)
Object	≤ 6	0.8	3×10^{14}	≥ 400	20
Reference	0.06	0.8	2.5×10^{13}	30	100
Probe	N/A	0.42	$\leq 10^{13}$	N/A	40

first-order probe intensities [Figs. 2(a), 2(b)] faithfully reconstruct the Gaussian and hollow ring profiles. Tilting the spiral phase plate shifts the ring position [see Fig. 2(b)], confirming sensitivity to wavefront variations. The probe focus was systematically scanned along the longitudinal x axis to sequentially capture information stored in consecutive transverse slices. These individual slices were subsequently decoded to extract temporally resolved transverse spatial information, which was then computationally combined to achieve complete spatiotemporal reconstruction. Detailed explanations of this methodology can be found in Section 5.C. Figures 2(c) and 2(d) reveal the complete reconstructed spatiotemporal structure of both Gaussian and LG foci. To the best of our knowledge, this represents the first direct experimental measurement of an ultrashort laser's spatiotemporal far-field(focus) dynamics, whereas other approaches are either near-field (unfocused) [28,29] or indirect far-field measurements [30].

To enable single-shot measurements, the probe pulse was expanded through a pinhole to uniformly illuminate the entire hologram, as shown in Fig. 1(c). In this configuration, the spatiotemporal information of the object pulse is projected onto the CCD camera along both the longitudinal and transverse dimensions [Figs. 3(a), 3(b)], providing a new perspective for observing the light field as well as the nonlinear laser–plasma dynamics. The reference pulse delay was precisely controlled via a delay line (see Section 5.B for experimental details), creating variable intersection points with the object pulse that facilitate spatiotemporal imaging at different spatial locations. Comparative analysis of these images enables direct observation of ultrafast propagation dynamics for both Gaussian and Laguerre–Gaussian (LG) beams in the gas-plasma medium. Figure 3 shows representative object-light images at four positions near the focal region for propagation analysis. For the Gaussian beam [Fig. 3(a)], we observed the characteristic focus–defocus sequence, revealing its nonlinear propagation behavior. The LG beam displayed distinct vortex dynamics: its asymmetric ring structure split into two lobes in the upper and lower regions, as shown in Fig. 3(b). Side illumination of the probe revealed the typical hollow intensity profile, confirming orbital angular momentum preservation. Notably, the vortex focus maintained a larger spot size and exhibited extended propagation without divergence compared to the Gaussian case, highlighting its unique propagation properties in the gas-plasma mixture.

To demonstrate the key innovation of our work—extending holography to the temporal dimension—we conducted a detailed investigation of temporal information retrieval. First, we systematically varied the object pulse duration τ by adjusting the grating distance D in the Ti:Sapphire laser system. For a chirped pulse, the duration is approximately given by $\tau \approx kD$, where $k \approx 1$ ps/mm^2 is a system-dependent coefficient and D represents the grating displacement from the zero-chirp position. By setting input pulse durations of 0.4, 0.8, and 1.1 ps, we successfully retrieved corresponding durations of 0.4, 0.75, and 1.0 ps, as shown in Fig. 4(a), respectively, confirming the plasma hologram's ability to accurately record pulse durations. Moreover, we examined the fine temporal structure by focusing the probe to a single point in the plasma grating and scanning the reference pulse delay. This approach, analogous to a scanning second-order autocorrelator, allowed us to reconstruct the temporal profile of the object pulse. Remarkably, the single-shot measurement at $\tau = 0.75$ ps showed excellent agreement with the scanning results [Fig. 4(b)], further validating the temporal resolution of our technique.

Second, we demonstrate precise control and retrieval of the object pulse's fine temporal structure through spectral manipulation. The object pulse's inherent multi-peak spectrum, resulting from resonator mode-locking, was modified by introducing a spectral blocker positioned between the compressing grating pairs in our laser system. As shown in Fig. 4(c), this blocker selectively

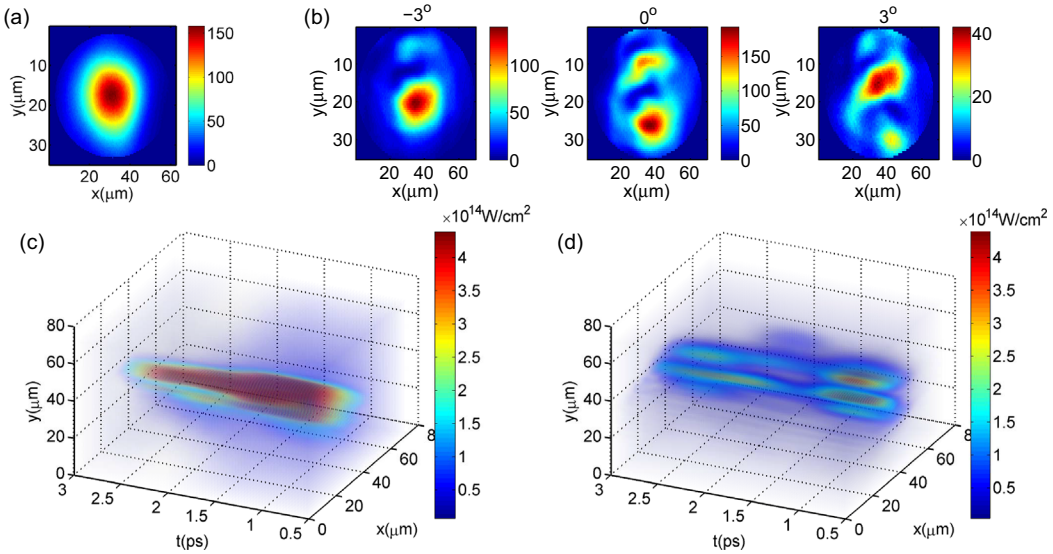

Fig. 2. Retrieved transverse intensity distribution of a Gaussian (a) and a Laguerre–Gaussian (b) object pulse. Reconstructed 3D spatiotemporal profiles of a Gaussian (c) and a Laguerre–Gaussian (d) object pulse by scanning measurements with a focused probe.

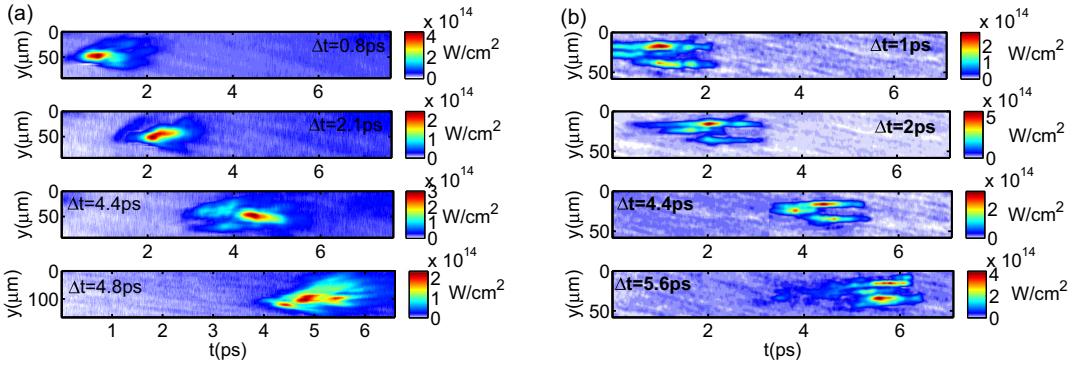

Fig. 3. Propagation process of a Gaussian object pulse (a) and a Laguerre–Gaussian pulse (b) in plasma by single-shot measurements. The label in each panel denotes the corresponding delay of the reference pulse.

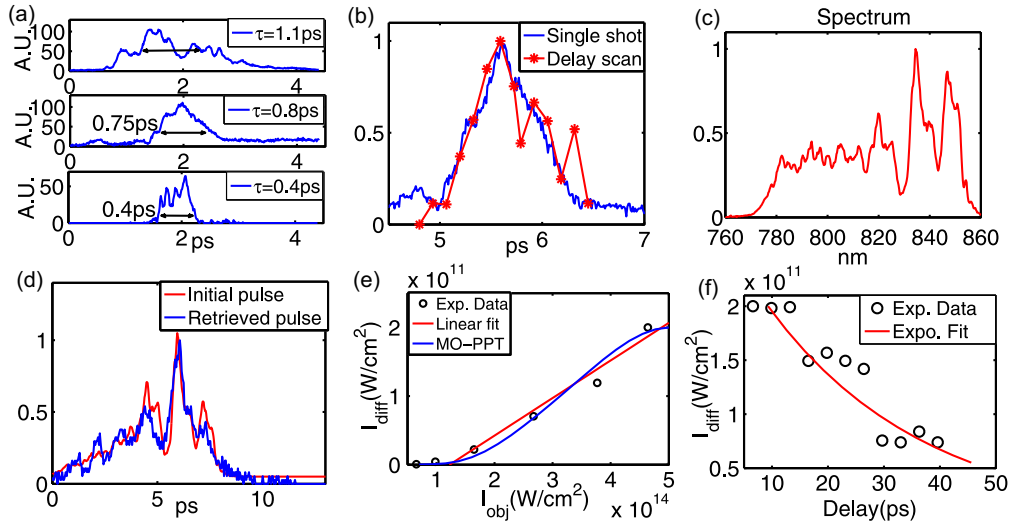

Fig. 4. (a) Retrieved temporal shape of the object pulse with different pulse durations. (b) Normalized temporal shape of the object pulse via single-shot and multi-shot measurements. (c) The processed object spectrum. (d) The fine temporal structures of the original object pulse (red curve) and retrieved object pulse (blue curve). (e) The diffracted probe intensities from experiments (scattered dots with red curve showing linear fit) compared with calculations based on the MO-PPT model and Eq. (2) (blue curve) for different input object intensities. (f) Experimentally measured diffracted probe intensities at different probe delays.

attenuated the first half of the spectral components while preserving the latter half. Using the known chirp rate ($k \approx 1\ \mathrm{ps/mm^2}$), we calculated the resulting temporal profile, revealing a distinctive trident-shaped waveform with ~ 4 ps duration [red curve, Fig. 4(d)]. Remarkably, this complex temporal structure was faithfully encoded in the plasma hologram and subsequently reconstructed. The excellent agreement between the retrieved waveform [blue curve, Fig. 4(d)] and the original temporal profile provides definitive evidence that volume plasma holography can capture and reproduce intricate temporal features of intense laser pulses.

Thus far, we have shown that plasma holograms generated through SVI can effectively store and retrieve both spatial and temporal information. To evaluate the robustness of this approach, at first, we systematically varied the object pulse intensity across a wide range 0.5×10^{14}–$5 \times 10^{14}\ \mathrm{W/cm^2}$. Successful information retrieval was achieved throughout this entire intensity range, confirming the technique's reliability. As shown in Fig. 4(e), the diffracted intensity exhibits an approximately linear dependence on object intensity, reaching a maximum diffraction efficiency of 2% at the highest object pulse intensity of $4.6 \times 10^{14}\ \mathrm{W/cm^2}$. These observations are in excellent agreement with our complete numerical calculation with MO-PPT model and Eq. (2) (blue curve). Within the experimental intensity range employed in our study, the ionization process predominantly involves removal of the outermost electron from both nitrogen and oxygen molecules. While plasma gratings may persist at higher intensities involving more and even inner-shell ionization, this regime introduces additional complexity that warrants separate investigation.

The hologram lifetime is a critical parameter for determining storage duration, retrieval efficiency, and potential applications such as optical buffering or flash memory. By systematically varying the probe pulse delay, we observed a clear decay in diffracted intensity, primarily attributed to plasma diffusion. This process gradually erases the density modulation $\Delta n(\mathbf{r})$ as electrons diffuse from high- to low-density regions, ultimately leading to grating collapse [24]. During ionization by a nonrelativistic laser, electrons are stripped from atoms and acquire significant transverse momentum along the laser polarization direction depending on the details of the laser field, resulting in a highly anisotropic plasma with much higher transverse temperature than the longitudinal temperature $T_\perp \gg T_\parallel$ [31–33]. Similarly, the longitudinal electron

temperature in our work can be estimated by equating the average longitudinal electron momentum $m_e\overline{v_\parallel}$ with the ponderomotive force impulse $f_p t_r \sim k_0\, m_e c^2 a_0 a_1 t_r$ during pulse overlap, where $a_{0,1}$ are the normalized vector potentials of the object and reference pulse, k_0 and ω_0 are the wavenumber and frequency of the object pulse, and t_r is the reference pulse duration. Using the parameters in Table 1, we estimate a low longitudinal electron temperature of $T_\parallel \approx 2.09$ eV. The subsequent thermal diffusion occurs at the ion sound speed $C_s \approx \sqrt{Z_N T_\parallel / m_N} \approx 1.26 \times 10^{-5} c$, with $Z_N = 1$ for nitrogen and m_N being the nitrogen mass. The total grating lifetime, defined as the time required for plasma to fill the inter-grating space and flatten the density perturbation [24], is estimated as $t_{\text{life}} \approx \Lambda / 2C_s \approx 52.9$ ps. This theoretical prediction shows reasonable agreement with the observed diffraction intensity decay in Fig. 4(f), validating our understanding of the plasma dynamics governing hologram persistence.

4. CONCLUSION

In conclusion, we have demonstrated the realization of a spatiotemporal plasma hologram based on spatially varying ionization, supported by a comprehensive theoretical model. Our experiments achieve reliable storage and retrieval of spatiotemporal information through two distinct probing schemes: multi-shot measurements with a scanned focused probe and single-shot measurements with an expanded probe. The capability to encode and reconstruct temporal information positions this plasma hologram as a promising candidate for ultrafast optical memory applications. Beyond simple storage, the system's unique properties—particularly the cumulative ionization response—open new possibilities for optical analogs of electronic circuits, such as differentiators and integrators. These functionalities would allow ultrafast mathematical operations on laser pulse shapes with exceptionally high repetition rates, leveraging the rapid recovery of the gaseous medium. Future developments may expand its operational intensity range, enhance diffraction efficiency, and explore more complex signal processing functionalities.

As the present work emphasizes temporal information reconstruction, the retrieved phase was not measured. However, as supported by prior theoretical and numerical studies [8,9]—as well as our theoretical modeling—the phase information has been retrieved by the probe pulse in the experiments here. In principle, the phase of the readout probe can be determined through multiple approaches. For example, interference between the diffracted zero-order probe and the first-order information-carrying probe would produce a characteristic fork-shaped pattern, enabling phase characterization. Alternatively, a Shack–Hartmann wavefront sensor could directly measure the twisted phase profile of the diffracted probe [34]. These phase-sensitive techniques may help to enable full spatiotemporal characterization of retrieved pulses in future studies.

5. MATERIALS AND METHODS

A. Time-Integrated Ionization Probability Calculation

The ionization probability was derived from the molecular Perelomov–Popov–Terentév (MO-PPT). The MO-PPT model is widely used for the calculation of the optical ionization for gases, it agrees well with the multiphoton ionization with a low laser intensity and the ADK model with a high laser intensity. Here, avalanche ionization is ignored because electron temperature is very low ($T_\parallel \approx 2.09$ eV). According to the MO-PPT model, the cycle-averaged ionization probability rate of a single molecule per unit time is given as

$$w = \left(\frac{3F}{\pi\kappa^3}\right)^{1/2} \frac{B^2(m) A_m(\omega, \gamma)}{2^m m! \kappa^{2Z_c/\kappa - 1}} \times \left[\frac{2\kappa}{F(1+\gamma^2)}\right]^{2Z_c/\kappa - m - 1} e^{\frac{-2\kappa^3 g(\gamma)}{3F}}, \tag{3}$$

where

$$g(\gamma) = \frac{3}{2\gamma}\left[\left(1 + \frac{1}{\gamma^2}\right)\sinh^{-1}\gamma - \frac{\sqrt{1+\gamma^2}}{2\gamma}\right] \tag{4}$$

with the Keldysh parameter $\gamma = \sqrt{I_p/U_p} = \sqrt{2I_p}\omega/F$, I_p is the ionization potential of the considered atom and U_p is the ponderomotive energy, F is the electric field strength, ω is the laser frequency, Z_c is the asymptotic charge, $\kappa = \sqrt{I_p/I_H}$ and I_H is the ionization potential of hydrogen. For a nonlinear molecule,

$$B(m) = \sum C_{lm} Q(l, m), \tag{5}$$

$$Q(l, m) = (-1)^{(m+|m|)/2} \sqrt{\frac{(2l+1)(l+|m|)!}{2(l-|m|)!}}, \tag{6}$$

where $A_m(\omega, \gamma)$ is given in Refs. [35–37], and C_{lm} can be found in Ref. [38].

Then, the time-integrated ionization probability P is

$$P = \int_0^\infty w \mathrm{d}t. \tag{7}$$

During the temporal overlap between the long object pulse and the short reference pulse (duration $t_r \approx 30$ fs, Gaussian profile), we compute the local ionization probabilities for both nitrogen and oxygen. Figure 5 reveals positive dependence of these probabilities on laser intensity across the range from 1×10^{13} to 1×10^{15} W/cm^2. Our results agree well with previous theoretical and numerical studies [16,17,39].

B. Experimental Setup

The experimental setup is shown in Fig. 6. An initial picosecond-duration laser pulse is provided by the Ti:Sapphire laser system, with a central wavelength of 800 nm and a bandwidth of 80 nm. The laser output was equally split into two pulses by a beam splitter BS1: one pulse with an energy up to 6 mJ was retarded by a delay line M3−M4, and then directly focused into the ambient air

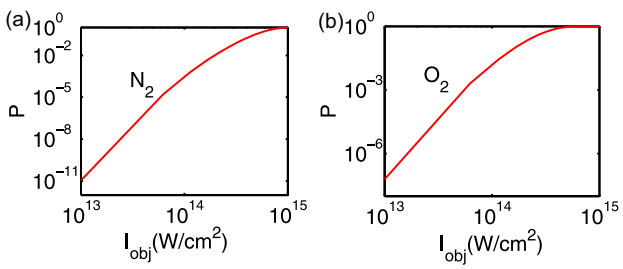

Fig. 5. Ionization probability of N_2 and O_2 for different laser intensities obtained by the MO-PPT model.

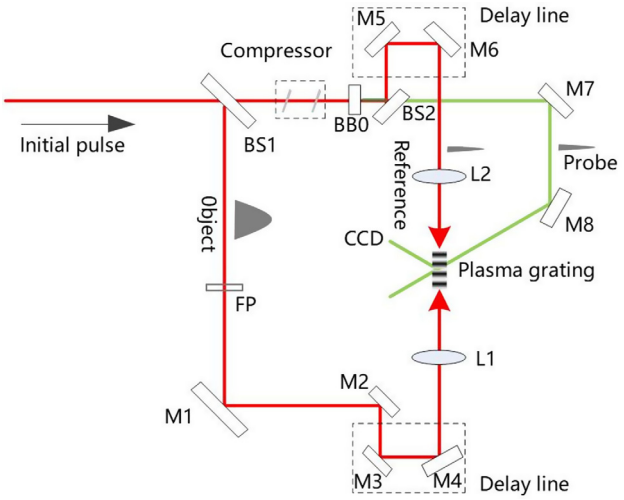

Fig. 6. Experimental setup for the spatiotemporal plasma hologram.

using an f/15 lens L1 as the object pulse. It had a full width at half-maximum (FWHM) focus diameter of ∼20 μm and a FWHM duration of several picoseconds. The peak focused laser intensity is around 3×10^{14} W/cm^2 by adjusting the pulse energy and duration. The other pulse was first compressed to approximately 30 fs by a pair of transmission gratings with grooves of 300/mm^2 and then partially doubled in frequency with a BBO crystal. A dichroic beam splitter BS2 then split it into a fundamental reference pulse (red) and a second-harmonic probe pulse (green). The reference pulse was adjusted by the delay line M5−M6, and then cut off to a diameter of 1 mm by an aperture. As a result, it had an energy of 60 μJ. It was then focused to overlap with the object focus using an f/100 lens L2, corresponding to a focused FWHM diameter ∼ 100 μm, and a focused intensity 2.5×10^{13} W/cm^2. Since the reference pulse's focus size was five times larger as that of the object pulse, the beam was nearly uniform within the interference region, ensuring that the plasma hologram only recorded information from the object pulse. Both the object and reference pulses had an adjustable delay line to precisely synchronize their timing. The probe pulse had a central wavelength of 420 nm and an FWHM spectral width of 10 nm. The duration of the probe cannot be measured by the autocorrelator but was estimated around ∼ 100 fs by the spectrum. However, the probe duration is not critical in the experiment because we only use its spatial distribution to show the spatiotemporal information of the object pulse. The pulse was directed toward the plasma grating at a Bragg angle of approximately 31.8°. The intensity is kept below 1×10^{13} W/cm^2 to avoid perturbing the plasma grating structure. The first-order diffracted pulse was then collected using a lens and imaged to a CCD camera for further analysis, with an imaging system magnification of approximately eight times. Given the CCD pixel size of 3.45 μm and the fact that the focal plane of the diffraction pattern was tilted by about 31.8° with respect to the propagation direction, each pixel corresponds to a lateral dimension of 0.45 μm and a longitudinal dimension of 0.9 μm.

In the experiment, the temporal coherent length is sufficiently long to match the object duration by using a 30 fs counter-propagating reference beam. The ultrashort reference beam exhibits a broad spectral bandwidth due to the Fourier-transform limit. During counter-propagation and scanning across the temporally extended object beam, spectral components maintaining phase coherence with the object beam are continuously available, as both beams originate from the same source with the object beam being chirped. This broadband characteristic enables the effective temporal coherence length be up to the duration of the object beam. Experimental verification was obtained by substituting the broadband 30 fs reference beam with a narrowband 400 fs version, which resulted in a significant reduction of the coherence length and consequently a much shorter plasma grating formation. Furthermore, the negligible spatial chirp in our experimental configuration ensures that the spatial coherence region remains comparable to the transverse dimensions of the object beam throughout the interaction process.

C. Respective Effects of Single-Shot and Scanning Images

In this study, the three-dimensional spatiotemporal information of the object beam is recorded in a volume plasma grating through interference-induced ionization between the object beam and the reference beam. The stored information is subsequently retrieved using a probe beam. However, as the probe pulse propagates obliquely through the plasma grating and is deposited on the two-dimensional CCD detector, one spatial dimension becomes integrated.

In the single-shot expanded probe configuration [see Fig. 7(a)], the probe illuminates the entire plasma grating, projecting the three-dimensional information onto a two-dimensional CCD with one transverse spatial dimension integrated while focusing on reading out the temporal information. Conversely, in the multi-shot scanning focused probe configuration [see Fig. 7(b)], the focused probe beam sequentially illuminates thin slices of the plasma grating (highlighted in red, yellow, and blue) during consecutive shots. The diffracted probe beams captured by the CCD camera are then decoded for temporally resolved two-dimensional transverse spatial information, which are then combined to achieve a complete three-dimensional reconstruction of the object beam. The two methodologies exhibit distinct performance characteristics with regard to spatiotemporal resolution capabilities and potential application domains.

1. Spatial Resolution

Both techniques are subject to identical constraints imposed by several factors. The primary resolution limit is governed by the diffraction-limited performance of the imaging system, as characterized by the Airy disk diameter $1.22\lambda f/D_l$, where λ is the probe wavelength, f is the focal length, and D_l is the lens aperture. Using the experimental parameters $\lambda = 0.42$ μm, $f = 100$ mm, and $D_l = 50$ mm, the diffraction-limited resolution is ∼0.26 μm. In addition, the finite CCD pixel size introduces a practical limitation. With a magnification of ∼8× and a pixel pitch of 3.45 μm, the effective spatial resolution is ∼0.45 μm, which dominates under our experimental conditions.

In addition to the imaging system, the plasma grating itself and the diffraction readout process are also considered. The plasma grating is formed by two counter-propagating 800 nm pulses, resulting in a period $\Lambda \approx 400$ nm. The object information is encoded in the slowly varying envelope of the plasma density modulation, while the grating period serves as a carrier that determines the Bragg diffraction condition. Consequently, the grating period can be regarded as a fundamental lower limit for spatial

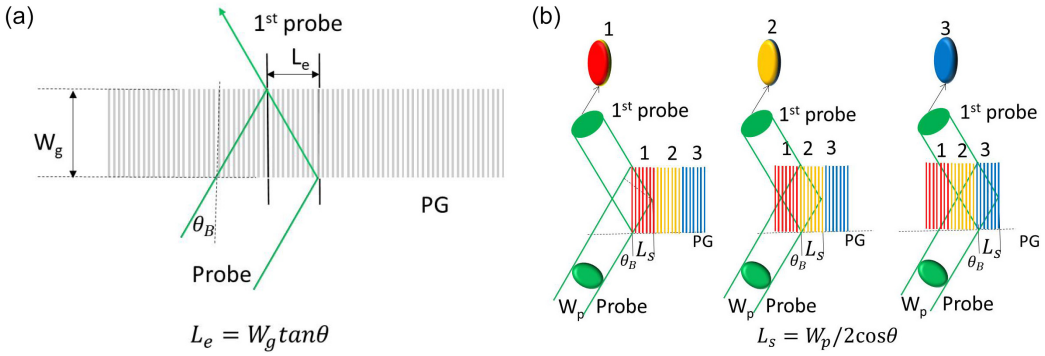

Fig. 7. Schematic diagrams illustrating the information readout process using (a) a single expanded probe and (b) multiple focused probes.

sampling ($\sim\Lambda = 400$ nm). For the probe readout, the finite bandwidth introduces a wavelength-dependent Bragg angle. While this would lead to angular dispersion in a non-imaging system, the plasma grating plane and the CCD plane in our setup satisfy an imaging relationship. As a result, different spectral components that are overlapped at the object plane remain co-localized at the image plane after imaging, and any spatial separation or mixing of signals from different object positions is insignificant. The influence of diffraction-related effects associated with the probe bandwidth on the spatial resolution is expected to be negligible under the present experimental conditions.

In summary, the effective spatial resolution is determined by the diffraction limit of the imaging system, the CCD pixel size, and the grating period, with the CCD pixel size being the dominant factor in the present experiment.

2. Temporal Resolution

The temporal resolution of the system is fundamentally constrained by two primary factors. The initial limitation arises from the ~30 fs reference pulse duration during the plasma grating formation process. The second constraint originates from the information retrieval mechanism, which differs between the expanded single-shot probe and focused scanning probe configurations.

As depicted in Fig. 7(a), for the expanded single-shot probe configuration, each diffracted ray originates from an effective plasma volume with thickness $L_e = W_g \tan\theta_B$, where W_g represents the grating diameter. This geometry imposes a temporal resolution limit of $\tau_e = L_e/c = W_g \tan\theta_B/c$, as the system cannot resolve temporal variations within the L_e interaction length. In contrast, the focused scanning probe configuration employs sequential interrogation of discrete plasma grating cross-sections (labeled 1, 2, 3,...), as shown in Fig. 7(b). Here, the temporal resolution is determined by the effective interaction thickness $L_s = W_p/(2\cos\theta_B)$, where W_p is the probe beam waist, yielding $\tau_s = L_s/c = W_p/(2c\cos\theta_B)$. This analysis reveals an inverse relationship between temporal resolution and probe aperture size. Using the experimental parameters listed in Table 1 ($W_e \approx 20$ μm, $W_p \approx 40$ μm, $\theta_B \approx 30°$), the temporal resolutions of the expanded single-shot probe and the scanning focused probe are estimated to be 38.5 and 77 fs, respectively, according to the corresponding expressions.

3. Application Domains

The two methodologies exhibit complementary characteristics that define their respective application domains. The focused scanning probe technique enables comprehensive three-dimensional reconstruction of laser pulse characteristics. However, this approach necessitates multiple laser exposures to acquire and computationally synthesize a sequence of cross-sectional profiles, thereby requiring a laser system with both high repetition rate and exceptional shot-to-shot stability.

Conversely, while the expanded single-shot probe configuration does not provide complete three-dimensional reconstruction capability, it offers distinct advantages for temporal holography applications. This includes precision measurement of pulse duration at the laser focus, temporal waveform characterization, and transient optical information storage. Notably, this single-shot technique maintains its effectiveness even when applied to low-repetition-rate or inherently unstable laser systems.

Funding. President's Fund of the China Academy of Engineering Physics (JCXYZ20260038); Natural Science Foundation of Guangdong Province (2025A1515012853); National Natural Science Foundation of China (12475248); Natural Science Foundation of Top Talent of SZT (GDRC202310); Shenzhen Key Laboratory of Ultraintense Laser and Advanced Material Technology (ZDSYS20200811143600001).

Acknowledgment. Zhaohui Wu proposed the idea and carried out the experiment. Hao Peng established the theoretical model. All authors built the experimental setup, data processing, and contributed to the paper.

Disclosures. The authors declare no competing interests.

Data availability. The data that support the findings of this study are available from the corresponding author upon reasonable request.

REFERENCES

1. C. Zuo, J. Qian, S. Feng, *et al.*, "Deep learning in optical metrology: a review," Light Sci. Appl. **11**, 39 (2022).
2. D. Pi, J. Liu, and Y. Wang, "Review of computer-generated hologram algorithms for color dynamic holographic three-dimensional display," Light Sci. Appl. **11**, 231 (2022).
3. T. Tahara, T. Shimobaba, and Y. Kozawa, "Review on imaging and sensing with holography," J. Opt. **27**, 043005 (2025).
4. M. Vassholz, H. Hoeppe, J. Hagemann, *et al.*, "Pump-probe X-ray holographic imaging of laser-induced cavitation bubbles with femtosecond FEL pulses," Nat. Commun. **12**, 3468 (2021).
5. H. Peng, J.-R. Marquès, L. Lancia, *et al.*, "Plasma optics in the context of high intensity lasers," Matter Radiat. Extrem. **4**, 065401 (2019).
6. C. Riconda and S. Weber, "Plasma optics: a perspective for high-power coherent light generation and manipulation," Matter Radiat. Extrem. **8**, 023001 (2023).

7. A. Leblanc, A. Denoeud, L. Chopineau, *et al.*, "Plasma holograms for ultrahigh-intensity optics," Nat. Phys. **13**, 440–443 (2017).
8. G. Lehmann and K. H. Spatschek, "Plasma volume holograms for focusing and mode conversion of ultraintense laser pulses," Phys. Rev. E **100**, 033205 (2019).
9. M. R. Edwards, V. R. Munirov, A. Singh, *et al.*, "Holographic plasma lenses," Phys. Rev. Lett. **128**, 065003 (2022).
10. I. Y. Dodin and N. J. Fisch, "Storing, retrieving, and processing optical information by raman backscattering in plasmas," Phys. Rev. Lett. **88**, 165001 (2002).
11. I. Dodin and N. Fisch, "Dynamic volume holography and optical information processing by raman scattering," Opt. Commun. **214**, 83–94 (2002).
12. T. Baba, "Slow light in photonic crystals," Nat. Photonics **2**, 465–473 (2008).
13. K. Jamshidi, S. Preußler, A. Wiatrek, *et al.*, "A review to the all-optical quasi-light storage," IEEE J. Sel. Top. Quantum Electron. **18**, 884–890 (2011).
14. O. Katz and O. Firstenberg, "Light storage for one second in room-temperature alkali vapor," Nat. Commun. **9**, 2074 (2018).
15. H. Chen, Y. Yin, C. Tian, *et al.*, "Moving electron density gratings induced in the beat-wave field of two counterpropagating laser pulses," Phys. Plasmas **17**, 083112 (2010).
16. S.-F. Zhao, L. Liu, and X.-X. Zhou, "Multiphoton and tunneling ionization probability of atoms and molecules in an intense laser field," Opt. Commun. **313**, 74–78 (2014).
17. S.-F. Zhao, A.-T. Le, C. Jin, *et al.*, "Analytical model for calibrating laser intensity in strong-field-ionization experiments," Phys. Rev. A **93**, 023413 (2016).
18. S.-F. Zhao, A.-T. Le, C. Jin, *et al.*, "Kinetics model of femtosecond laser ionization in nitrogen and comparison to experiment," J. Appl. Phys. **125**, 243301 (2016).
19. V. S. Popov, "Tunnel and multiphoton ionization of atoms and ions in a strong laser field (Keldysh theory)," Phys. Usp. **47**, 855–885 (2004).
20. X. M. Tong and C. D. Lin, "Empirical formula for static field ionization rates of atoms and molecules by lasers in the barrier-suppression regime," J. Phys. B: At. Mol. Opt. Phys. **38**, 2593–2600 (2005).
21. Y. Zhou, R. Lock, W. Li, *et al.*, "Molecular recollision interferometry in high harmonic generation," Phys. Rev. Lett. **102**, 073902 (2009).
22. P. Yeh and W. Moerner, *Introduction to Photorefractive Nonlinear Optics* (Wiley, 1994).
23. M. Durand, A. Jarnac, Y. Liu, *et al.*, "Dynamics of plasma gratings in atomic and molecular gases," Phys. Rev. E **86**, 036405 (2012).
24. C. Zhang, Z. Nie, Y. Wu, *et al.*, "Ionization induced plasma grating and its applications in strong-field ionization measurements," Plasma Phys. Control. Fusion **63**, 095011 (2021).
25. M. R. Edwards and P. Michel, "Plasma transmission gratings for compression of high-intensity laser pulses," Phys. Rev. Appl. **18**, 024026 (2022).
26. M. R. Edwards, N. M. Fasano, A. M. Giakas, *et al.*, "Greater than five-order-of-magnitude postcompression temporal contrast improvement with an ionization plasma grating," Phys. Rev. Lett. **133**, 155101 (2024).
27. M. R. Edwards, S. Waczynski, E. Rockafellow, *et al.*, "Control of intense light with avalanche-ionization plasma gratings," Optica **10**, 1587–1594 (2023).
28. K. Nakagawa, A. Iwasaki, Y. Oishi, *et al.*, "Sequentially timed all-optical mapping photography (STAMP)," Nat. Photonics **8**, 695–700 (2014).
29. H. Tang, T. Men, X. Liu, *et al.*, "Single-shot compressed optical field topography," Light Sci. Appl. **11**, 244 (2022).
30. A. Jarnac, G. Tamosauska, D. Majus, *et al.*, "Whole life cycle of femtosecond ultraviolet filaments in water," Phys. Rev. A **89**, 033809 (2014).
31. C.-K. Huang, C.-J. Zhang, K. A. Marsh, *et al.*, "Initializing anisotropic electron velocity distribution functions in optical-field ionized plasmas," Plasma Phys. Control. Fusion **62**, 024011 (2020).
32. C. Zhang, C.-K. Huang, K. A. Marsh, *et al.*, "Ultrafast optical field–ionized gases—a laboratory platform for studying kinetic plasma instabilities," Sci. Adv. **5**, eaax4545 (2019).
33. C. Zhang, J. Hua, Y. Wu, *et al.*, "Measurements of the growth and saturation of electron Weibel instability in optical-field ionized plasmas," Phys. Rev. Lett. **125**, 255001 (2020).
34. B. C. Platt and R. Shack, "History and principles of Shack-Hartmann wavefront sensing," J. Refract. Surg. **17**, S573–S577 (2001).
35. F. A. Ilkov, J. E. Decker, and S. L. Chin, "Ionization of atoms in the tunnelling regime with experimental evidence using Hg atoms," J. Phys. B: At. Mol. Opt. Phys. **25**, 2005 (1992).
36. Y. Z. Fu, S.-F. Zhao, and X. X. Zhou, "Multiphoton and tunneling ionization of atoms in an intense laser field," Chin. Phys. B **21**, 113101 (2012).
37. A. M. Perelomov, V. S. Popov, and M. V. Terentèv, "Ionization of atoms in an alternating electric field," Sov. Phys. JETP **23**, 924 (1966).
38. X. M. Tong, Z. X. Zhao, and C. D. Lin, "Theory of molecular tunneling ionization," Phys. Rev. A **66**, 033402 (2002).
39. C. Guo, M. Li, J. P. Nibarger, *et al.*, "Single and double ionization of diatomic molecules in strong laser fields," Phys. Rev. A **58**, R4271–R4274 (1998).